Research Article

Open Access

Image Stitching for Achilles Tendon Ultrasonography Using Particle Swarm Optimization of Boundary Vector Field Based Similarity and Log-Domain Diffeomorphic Registration

Jingyu Xiong[1,2], Qi Zhang[1,2*], Jingfeng Suo[2], Yehua Cai[3], Jun Shi[1,2] and Yinghui Hua[4]

[1] *Shanghai Institute for Advanced Communication and Data Science, Shanghai University, Shanghai, China*

[2] *School of Communication and Information Engineering, Shanghai University, Shanghai, China*

[3] *Department of Ultrasound, Huashan Hospital, Fudan University, Shanghai, China*

[4] *Department of Sports Medicine, Huashan Hospital, Fudan University, Shanghai, China*

*Correspondence to:
Qi Zhang
School of Communication and Information
Engineering, Shanghai University
Shanghai, China
Tel: +86-21-66137256
E-mail: zhangq@t.shu.edu.cn

Abstract

Objective: The Achilles tendon (AT) is the longest and strongest tendon in the human body. Ultrasound (US) imaging including B-mode US and sonoelastography is valuable for examination of AT. Due to its long length, the AT is often divided into multiple successive and overlapping sections for US scanning. We aim to propose a coarse-to-fine method for image stitching of these multiple US scans.

Methods: First, a new similarity measure for rigid registration is proposed based on the boundary vector field, and it is maximized by using the particle swarm optimization for coarse alignment. Second, the log-domain diffeomorphic registration is followed for non-rigid refinement. Finally, the weighted averaging is utilized for image blending.

Results: Simulation experiments of non-rigid registration on 20 image pairs show that the horizontal, vertical and distance registration errors of our method are 1.422, 0.628, and 1.616 pixel, respectively. Non-rigid registration experiments on 11 pairs of real clinical US images demonstrate that the horizontal, vertical and distance registration errors are 1.514, 1.205, and 1.928 pixel, respectively. Registration results on both synthetic images and real clinical images by our method exceeded those of other four methods. After image blending on multiple AT sections of US scans, panoramas of AT are generated for dual modality visualization of both B-mode and sonoelastography.

Conclusions: Our technique can accurately stitch multiple sections of both B-mode and elastographic US scans and provide panoramas of AT, which may help diagnosis and treatment evaluation of tendinopathies and tendon ruptures.

Keywords

Achilles tendon, Log-domain diffeomorphic registration, Image stitching, Non-rigid registration, Ultrasound, Sonoelastography

Introduction

The Achilles tendon (AT) is the longest and strongest tendon in the human body [1, 2]. AT injuries consist of Achilles tendinopathies and tendon ruptures, which can dramatically affect the life quality of a patient [3, 4]. Making an accurate diagnosis and identifying the location and extent of the AT injuries is an essential step toward formulating effective treatment plan and evaluating prognosis. B-mode ultrasound (US) is beneficial in the AT examination, thanks to its realtime image acquisition, high safety, low cost and wide availability [5]. Sonoelastography (SE)

Image Stitching for Achilles Tendon Ultrasonography Using Particle Swarm Optimization of Boundary Vector Field Based Similarity and Log-Domain Diffeomorphic Registration

Xiong et al.

is a new development of ultrasonography for assessment of tissue elasticity by measuring tissue strain or shear-wave speed. There has been increasing interest in SE for AT imaging [6, 7]. In addition to B-mode US, SE of AT provides supplementary information regarding its biomechanical properties [8, 9].

Due to the long length of AT and the limited length of a US probe, US examination of AT is divided into multiple successive and overlapping scans. Thus, it is not accurate and convenient for comprehensively assessing the severity and extent of AT injuries. Image stitching of US scans can provide a panorama of AT, presenting its complete structure and elastic function.

Image stitching technologies consist of two steps, image registration and image blending [10-12]. The image registration can be classified into rigid registration and non-rigid registration. Rigid registration aligns, and matches overlap regions on two images exhibiting rigid deformation, which includes translation and rotation and is the most fundamental transform in medical images. Non-rigid registration rectifies the non-rigid deformation between two images. Tendons are elastic tissues, and their elongation and contraction produce elastic deformations. Thus, a coarse-to-fine registration strategy, which consists of rigid registration for coarse alignment and a following non-rigid registration for refinement, seems promising for image stitching of AT ultrasonography. The image blending technique is used for correcting the grayscale and color differences and suppressing the seam-line between stitched images to yield seamless stitching.

Commercial SE imaging systems often provide dual-modality visualization, simultaneously displaying a color elastic image along with a grayscale B-mode image, as shown in figure 1a. Thus, it is needed to effectively and accurately stitch both B-mode and elastographic images of AT. We propose a coarse-to-fine method for image stitching of multiple US scans. First, the rigid registration for coarse alignment is conducted with a new similarity measure based on the boundary vector field (BVF), which is maximized by using the particle swarm optimization (PSO). Second, the non-rigid registration is followed for transform refinement using the log-domain diffeomorphic registration [13]. Finally, the image blending is performed with the weighted averaging approach.

Methods

Rigid registration using PSO of BVF-based similarity

The rigid registration is composed of three components, the feature space, similarity measure, and search strategy. The feature space is the data space that the registration relies on, which can be either all pixels in an image, or representative features extracted from an image. According to their feature space, the registration methods can be classified into two categories, the pixel-based and the feature-based methods [14-16]. The similarity measure is an index quantifying the similarity between two images, which is generally cross-

correlation, mutual information or a distance measure. The search strategy is used for seeking the optional transform between two images while maximizing their similarity measure. Since exhaustive search is very time consuming, it is necessary to maximize the similarity measure by optimization algorithms.

In the dual-modality visualization, B-mode image is spatially matched with the SE image (Figure 1a). Because the B-mode image has higher spatial resolution and depicts more tissue structures, the image registration is conducted only on B-mode US to determine the transform between two images. Then the SE image is also aligned using the same transform.
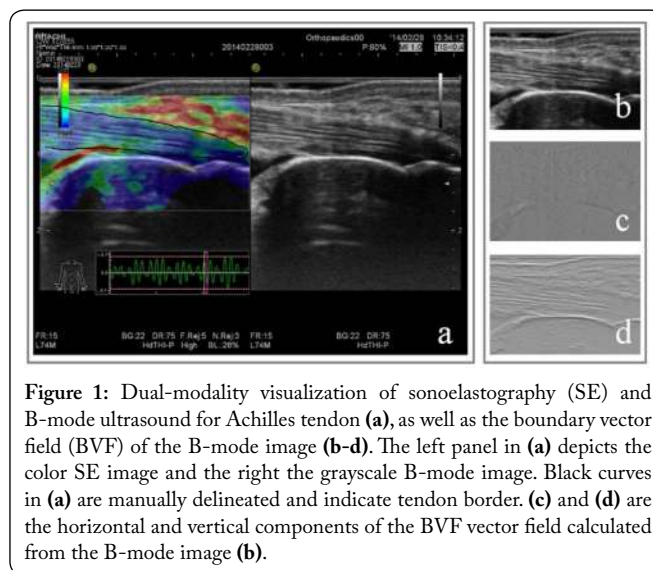

Figure 1: Dual-modality visualization of sonoelastography (SE) and B-mode ultrasound for Achilles tendon **(a)**, as well as the boundary vector field (BVF) of the B-mode image **(b-d)**. The left panel in **(a)** depicts the color SE image and the right the grayscale B-mode image. Black curves in **(a)** are manually delineated and indicate tendon border. **(c)** and **(d)** are the horizontal and vertical components of the BVF vector field calculated from the B-mode image **(b)**.

Feature Space. We propose a hybrid algorithm combining pixel-based and the feature-based methods. We derive an edge-strengthened image, called a feature image, and use all pixels in the image as the feature space of the rigid registration. Here we introduce a robust image feature, namely the BVF [17], which can not only enhance tissue edges and suppress speckle noise, but also have a minor varying field in homogeneous regions. Thus, it might be robust when used as the feature space.

The BVF field was initially proposed for image segmentation [17]. It is a vector field derived from an image $I(x, y)$ and is comprised of 2-D vectors towards tissue edges. In order to calculate BVF, a boundary map is first computed as the convoluted image of $I(x, y)$ via Gaussian filtering. The boundary map is converted to a binary map, from which two potential functions are interpolated using two independent line-by-line scans along horizontal and vertical directions, respectively. The BVF field $v_{BVF}(x, y) = [u(x, y), v(x, y)]$ is then calculated using the gradients of potential functions. Its horizontal component, $u(x, y)$, and vertical component, $v(x, y)$, emphasize the vertical and horizontal tissue edges, respectively, as shown in figure 1c and 1d.

From the perspective of feature extraction, the BVF retains and enhances the image edge features in noisy background, and the introduction of the minor varying field into homogeneous areas extends the coverage of the field.

Image Stitching for Achilles Tendon Ultrasonography Using Particle Swarm Optimization of Boundary Vector Field Based Similarity and Log-Domain Diffeomorphic Registration

Xiong et al.

Similarity Measure. The normalized mutual information (NMI) is a variant of mutual information, widely used in the pixel-based registration. However, the conventional NMI works on pixels of the original image and hence is sensitive to noise. Here we propose calculating NMI on BVF fields, called NMIBVF, to increase the robustness of NMI:

$$NMI_{BVF} = [H(u_1)+H(u_2)]/H(u_1, u_2)+[H(v_1)+H(v_2)]/H(v_1, v_2) \quad .....(1)$$

where $H(u_i)$ is the Shannon's entropy of the BVF horizontal component, and $H(v_i)$ is that of the vertical component; $i = 1$, 2, denoting the fixed image (i.e., reference image) and moving image (i.e., target image), respectively; $H(u_1, u_2)$ is the joint entropy of the two BVF horizontal components and $H(v_1, v_2)$ is that of the vertical components. When we transform the moving image by horizontal translation of t_x, vertical translation of t_y, and rotation of θ, denoted by a transform vector (t_x, t_y, θ), the NMIBVF between the fixed image (I_1) and the transformed moving image (I_3) is represented by $NMI_{BVF}(t_x, t_y, \theta)$. When $NMI_{BVF}(t_x, t_y, \theta)$ reaches maximum, the optimal transform vector (t_x, t_y, θ) is obtained.

Search Strategy. An ideal search strategy should be capable of accurately and quickly finding the optimal rigid transform (t_x, t_y, θ) between two images when the similarity measure reaches the maximum. PSO is a population-based evolutionary computation approach exploiting cooperative and social aspects of the biological phenomena [18-22]. It is an iterative method to move individuals (i.e., particles) in a population (i.e., a swarm) in the search space and eventually find the best solution.

Here we use a hybrid PSO method which integrates PSO with genetic algorithms [23]. After particle positions are updated at each iteration, particles are selected in pairs for crossover. The hybrid PSO enhances searching the space between particles. Via crossover, the searching may skip off from the local maxima and approach the global maximum.

Iterative Adjustment of Overlap Regions. For computational simplicity and reduction of interference from irrelevant tissues, the rigid registration is only conducted in overlap regions between the fixed and moving images. Therefore, we should localize the overlap regions in the two images. Here we propose an iterative approach to localize the overlap regions. Without loss of generality, suppose the right part of the fixed image I_1 and the left part of the moving image I_2 are overlapped. Let there be d columns in matrix I_1. The adjustment of overlap regions is performed as follows:

a) The right part of I_1 with $d_1 = \lfloor d \times n / m \rfloor$ columns are denoted by I_1' and recognized as the overlap region in I_1, and the left part of I_2 with d_1 columns is denoted by I_2' and recognized as the overlap region in I_2. Here, n and m are proportion factors, which are two integers initially set as 25 and 50, respectively. $\lfloor \cdot \rfloor$ represents the rounding up operation.

b) The horizontal displacement t_x is calculated by image registration between I_1' and I_2'.

c) Let $\Delta n = \lfloor t_x \times m / d \rfloor$. If $\Delta n \neq 0$, update n = n+ Δn and go back to step a; otherwise, move to step d.

d) Obtain the final overlap regions and the rigid transform between I_1 and I_2. The final overlap region on the fixed image is denoted as I_1' and that on the rigid transformed (i.e., coarse-aligned) moving image is denoted as I_3'.

Non-rigid registration using log-domain diffeomorphic algorithm

We employ a diffeomorphic non-rigid image registration algorithm coupled with the demons approach. The algorithm uses a Lie group structure, which defines an exponential mapping from a smooth velocity field to a diffeomorphism, i.e., represents the complete deformation as an exponential of the smooth velocity field [24]. Thus, it is called a log-domain diffeomorphic algorithm (LDDA). Moreover, it uses a demons-like optimization approach for efficiency [25, 26].

Our algorithm aims at finding a well-behaved spatial transformation s: z $\mapsto$ z+s(z), which defines a displacement field s(z) at each point z that optimally fine-aligns the fixed image I1 and the coarse-aligned moving image I3 to get the fine-aligned moving image I4. To reduce computational complexity and increase robustness, the algorithm is conducted in overlap regions I1' and I3' to get the fine-aligned overlap region I4'. The algorithm includes the following steps:

a) Choose a starting spatial transformation *s* that meets *s* = exp(*v*), where *v* is the log-domain displacement field (or called the velocity field), and exp() is the exponential operation that can be computed with a fast algorithm in a recursive manner [25].

b) Given the current transformation *s*, i.e., displacement field *s*(*z*), calculate an update velocity field *u* by minimizing an energy function $E(I_1', I_3', s, u)$ with respect to *u*:

$$E(I_1', I_3', s, u) = SIM(I_1', I_3', s \circ exp(u)) + ||u||^2 \quad ....(2)$$

where SIM(I_1', I_3', *s* $\circ$ exp(*u*)) = $|| I_1' - I_3' \circ s \circ exp(u)||^2/2$ is a similarity function and $\circ$ denotes the composition of functions.

c) Perform fluid-like regularization *u* $\leftarrow$ K_{fluid} * *u*, where K_{fluid} is a Gaussian kernel function and * is the convolution operation.

d) Updated the velocity field by $v \leftarrow v + u$.

e) Perform diffusion-like regularization *v* $\leftarrow$ $K_{diffusion}$ * *v*, where $K_{diffusion}$ is also a Gaussian kernel function.

f) If the iteration converges, stop here; otherwise, go back to step b.

g) When the non-rigid displacement field is determined, the overlap region on the moving image I_3' is transformed to get a fine-aligned overlap region I_4'. By using the interpolated non-rigid displacement field, the non-overlap region is transformed to get a fine-aligned non-overlap region I_4''.

Image blending

After registration, image blending is performed on both grayscale B-mode image and color SE image. Our image blending technique is comprised of two steps: the brightness/

Image Stitching for Achilles Tendon Ultrasonography Using Particle Swarm Optimization of Boundary Vector Field Based Similarity and Log-Domain Diffeomorphic Registration

Xiong et al.

color adjustment, and the seamless weighted averaging.

The fixed and moving images may have brightness difference in B-mode US and color difference in SE. Thus, the linear brightness/color adjustment is adopted to reduce the difference. For grayscale B-mode US, the highest and lowest intensities at overlap regions in the moving image are linearly adjusted to the same intensities in the fixed image. For color SE, the linear adjustment is employed on the intensity channel of the HSI (hue, saturation and intensity) space, while the other two channels remain unchanged, as shown in figure 2.

Figure 2: Color adjustment for sonoelastography. **(a)** Fixed image, **(b)** moving image, and **(c)** moving image after color adjustment.
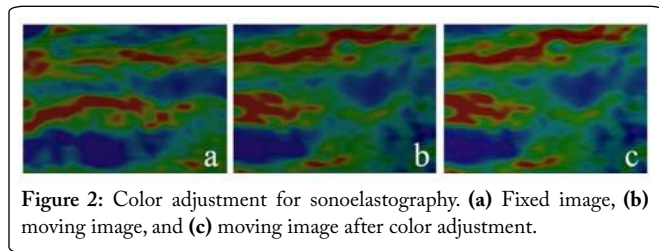
The weighted averaging method is performed at the overlap region I_1' on the fixed image and the fine-aligned overlap region I_4' on the moving image [27-29], as shown in figure 3. $I_s(z)$ is the intensity at pixel z on the blended image of overlap regions, which is the weighted average of $I_1'(z)$ and $I_4'(z)$, satisfying $I_s(z) = \alpha \times I_1'(z) + (1-\alpha) \times I_4'(z)$. Here, α is the weighting coefficient, and its value is linearly varied from 1 when stitching the far left on the overlap region to 0 when stitching the far right, hence leading to seamless blending and stitching.

Figure 3: Diagram for image blending with the seamless weighted averaging.
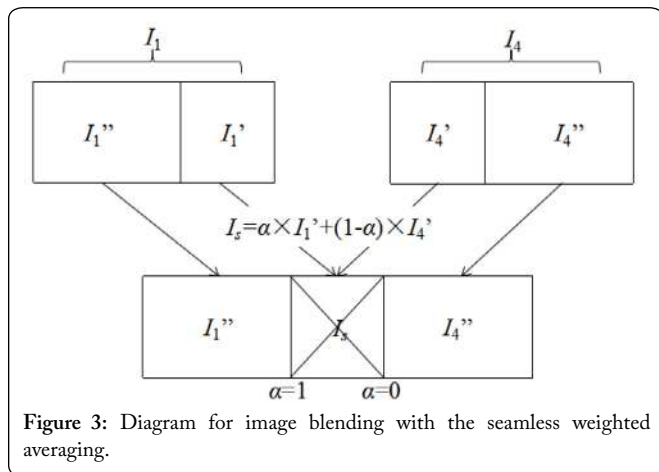
Experiments and Results

Experimental setup

Clinical dual modal AT images of both B-mode US and SE were acquired from nine patients with AT disorders at Huashan Hospital, Fudan University, Shanghai, China. The patients were examined using the HI VISION Preirus system (Hitachi Medical, Tokyo, Japan) equipped with a linear array transducer (L74 M, 5–13 MHz), while they were in a prone position with the foot hanging over the edge of the examination

bed. Both B-mode US and SE were performed on AT by a radiologist with 12 years of experience in musculoskeletal US. Twenty dual modal images were acquired with a resolution of 18 pixel/mm, where three overlapping images were acquired from each of two patients and two overlapping images were acquired from each of the other seven patients. All procedures were in accordance with the ethical standards of the institutional review board and informed consent was obtained from all individual participants included in the study.

Simulation work was first conducted by intentionally transforming a clinical image as a moving image to generate a synthetic fixed image so as to validate the presented registration method, denoted by PSOBVF-LDDA, and compare it with four other methods, namely LDDA (without rigid registration), PSOBVF (without non-rigid refinement), PSOBVF-FFD (non-rigid refinement using free-form deformation [FFD] instead), and FFD (without rigid registration, only FFD for non-rigid registration) [30]. In the simulation experiments, each of the 20 clinical images was used as a moving image to generate a synthetic fixed image. The simulation experiments of rigid transform and non-rigid transform were both performed on these 20 pairs of images for comprehensive evaluations. Because PSO was initialized with random particles, we conducted experiments of the algorithms involving PSO (namely PSOBVF, PSOBVF-FFD and PSOBVF-LDDA) 10 times to evaluate their performance.
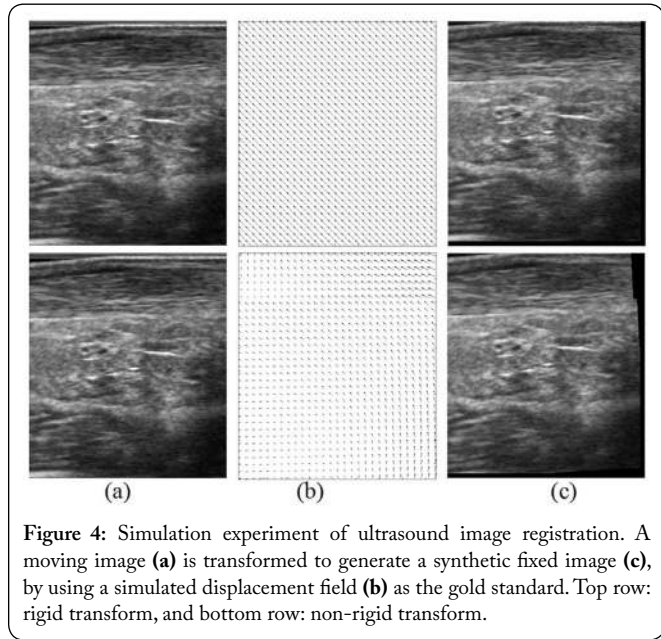
Experiments on real clinical images were also conducted. The coarse-to-fine registration and image stitching experiments were performed on two (or three if applicable) real clinical images for each patient. A patient with three overlapping images has two pairs of images for registration and a patient with two overlapping images has one pair. Thus, there are in total 11 pairs of clinical images for evaluation of the registration and stitching method. We conducted experiments of the algorithms involving PSO 10 times to evaluate their performance.

All the computerized experiments were implemented with MatlabR2014a (Mathworks, Natick, MA). Since exhaustive search is very time consuming in the hybrid PSO method, three rigid transform parameters (t_x, t_y, θ) were optimized by using the grid search limited in a range of [-25, 25] with an interval of 1 pixel or degree. We empirically set the number of particles to 24 and the maximal number of iterations to 30 to yield best performance.

Simulation experiments of rigid transform

A B-mode image, as a moving image, was horizontally and vertically shifted by p_0 and q_0 pixel respectively to generate a synthetic fixed image, as shown in figure 4(top row), and the applied displacements along horizontal and vertical directions, $P_g = (p_{g,i}, q_{g,i}) = (p_0, q_0)$, $i = 1, 2, ..., n$, served as the gold standard of image registration. Here n denoted the pixel number in an image. Five methods were used to register the two images before and after the rigid transform. The estimated displacement field was $P = (p_i, q_i)$. The horizontal (e_x), vertical (e_y), and distance (e_d) registration errors were defined as follows:

Image Stitching for Achilles Tendon Ultrasonography Using Particle Swarm Optimization of Boundary Vector Field Based Similarity and Log–Domain Diffeomorphic Registration

Xiong et al.

$$\begin{cases} e_x = \dfrac{1}{n}\sum_{i=1}^{n}\left|p_i - p_{g,i}\right| \\[2ex] e_y = \dfrac{1}{n}\sum_{i=1}^{n}\left|q_i - q_{g,i}\right| \\[2ex] e_d = \dfrac{1}{n}\sum_{i=1}^{n}\sqrt{\left(p_i - p_{g,i}\right)^2 + \left(q_i - q_{g,i}\right)^2} \end{cases} \quad \ldots\ldots\ldots\ldots (3)$$

Figure 4: Simulation experiment of ultrasound image registration. A moving image **(a)** is transformed to generate a synthetic fixed image **(c)**, by using a simulated displacement field **(b)** as the gold standard. Top row: rigid transform, and bottom row: non-rigid transform.

We set both p_0 and q_0 to different pixel in our experiments for mimicking the in vivo displacements. The results are listed in table 1. The methods with rigid registration (PSOBVF, PSOBVF-FFD and PSOBVF-LDDA) attained horizontal and vertical errors between 0.037 and 0.135 pixel, better than those without rigid registration (FFD and LDDA, 0.333 – 2.270 pixel). The distance errors of the methods with rigid registration (0.102 – 0.163 pixel) were also superior to those of the methods without rigid registration (2.178 – 2.371 pixel).

Table 1: Simulation results of rigid transform.

Methods	Displacement errors		
	e_x (pixel)	e_y (pixel)	e_d (pixel)
PSOBVF	0.108 ± 0.042	0.087 ± 0.036	0.141 ± 0.068
FFD	2.270 ± 0.977	0.333 ± 0.532	2.371 ± 1.108
LDDA	1.330 ± 0.980	0.794 ± 0.386	2.178 ± 1.058
PSOBVF-FFD	0.084 ± 0.028	0.037 ± 0.020	0.102 ± 0.031
PSOBVF-LDDA	0.092 ± 0.082	0.135 ± 0.077	0.163 ± 0.077

Simulation experiment of non-rigid transform

As shown in figure 4(bottom row), a B-mode image was transformed with a given non-rigid displacement field $P_g = (p_{g,i}, q_{g,i})$. The non-rigid displacement field was a composite field, which consists of a rigid component with both p_0 and q_0 equaling to 10 pixel and a non-rigid component mimicking tendon contraction and muscle twist.

The estimated displacement field P = (p_i, q_i) was derived by five methods. The displacement field estimated by PSOBVF-LDDA (Figure 5e, middle) was very similar to the gold standard (Figure 4b, bottom) and the difference image (Figure 5e, bottom) between the fixed image (Figure 4c, bottom) and the registered moving image (Figure 5e, top) was almost entirely black. These qualitative results were consistent with the small quantitative indices listed in table 2 (e_x = 1.422, e_y = 0.628, and e_d = 1.616 pixel). PSOBVF-FFD achieved the second best results with an e_d-value of 1.959 pixel, which were much better than other three methods. The comparison work show that both the rigid registration PSOBVF and the non-rid registration LDDA have contributed to the best performance of PSOBVF-LDDA.
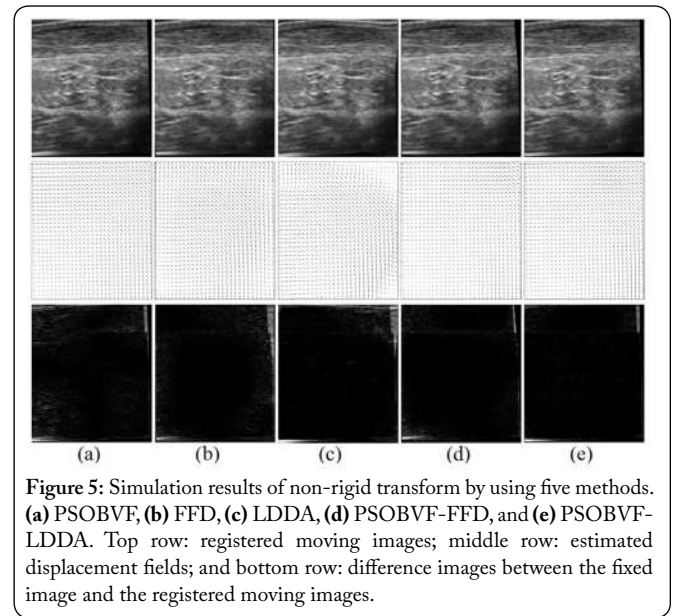

Figure 5: Simulation results of non-rigid transform by using five methods. **(a)** PSOBVF, **(b)** FFD, **(c)** LDDA, **(d)** PSOBVF-FFD, and **(e)** PSOBVF-LDDA. Top row: registered moving images; middle row: estimated displacement fields; and bottom row: difference images between the fixed image and the registered moving images.

Table 2: Simulation results of non-rigid transform.

Methods	Displacement errors		
	e_x (pixel)	e_y (pixel)	e_d (pixel)
PSOBVF	2.771 ± 0.489	1.535 ± 0.167	3.156 ± 0.191
FFD	3.125 ± 0.373	1.488 ± 0.392	3.969 ± 0.399
LDDA	3.134 ± 1.047	1.682 ± 0.956	3.998 ± 1.650
PSOBVF-FFD	1.692 ± 0.240	0.724 ± 0.176	1.959 ± 0.307
PSOBVF-LDDA	1.422 ± 0.306	0.628 ± 0.051	1.616 ± 0.294

Coarse-to-fine registration for real clinical images

Image registration was also performed on real *in vivo* clinical images. Taking figure 6 as an example, the three methods using rigid registration, namely PSOBVF (c), PSOBVF-FFD (f) and PSOBVF-LDDA (g), successfully recovered the rigid transform between the fixed and moving images, as illustrated by the yellow circle 1 (g). Furthermore, the hypoechoic strip in (g) indicated by yellow circle 2 was wider than those in (c) and (f), and the hypoechoic hole in (g) indicated by yellow circle 3 was larger than those in (c) and (f). Compared with PSOBVF (c) and PSOBVF-FFD (f), our method PSOBVF-LDDA (g) recovered these hypoechoic

Image Stitching for Achilles Tendon Ultrasonography Using Particle Swarm Optimization of Boundary Vector Field Based Similarity and Log-Domain Diffeomorphic Registration

Xiong et al.

regions more similar to those in the fixed image (a), indicating that the refined non-rigid registration by LDDA captured more details and performed better than FFD and the scheme without non-rigid refinement.
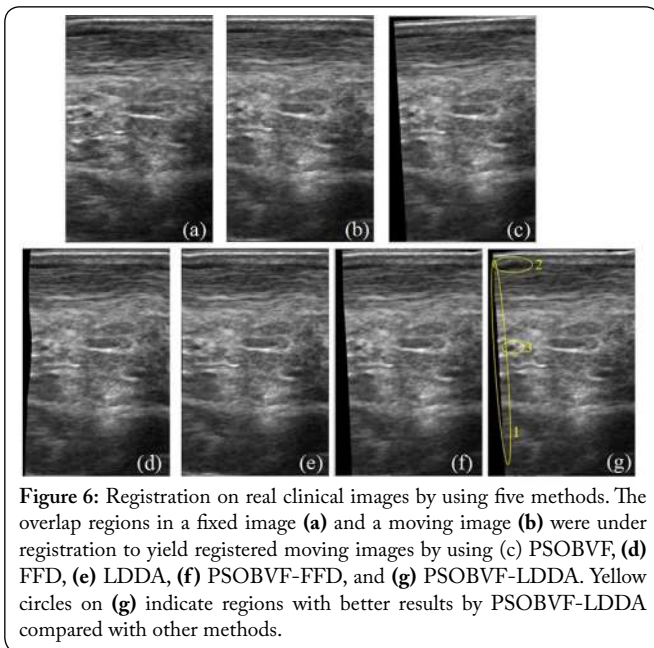

Figure 6: Registration on real clinical images by using five methods. The overlap regions in a fixed image **(a)** and a moving image **(b)** were under registration to yield registered moving images by using (c) PSOBVF, **(d)** FFD, **(e)** LDDA, **(f)** PSOBVF-FFD, and **(g)** PSOBVF-LDDA. Yellow circles on **(g)** indicate regions with better results by PSOBVF-LDDA compared with other methods.

The displacement field between two real clinical images is unknown. In order to determine the registration errors, several points were marked manually in pairs on both the fixed (Figure 7a) and moving (Figure 7) (b) clinical images, and then the marked points on the moving image were automatically mapped to the registered moving image (Figure 7c) according to the estimated displacement field. The registration errors e_x, e_y, and e_d were calculated via Equation (3) based on the distance between the paired markers in the fixed image and registered moving image, where n denoted the number of paired markers. Table 3 enumerates the results of clinical image registration. Our method PSOBVF-LDDA had e_x-, e_y-, and e_d-values of 1.514, 1.205 and 1.928 pixel, demonstrating high precision and superiority to the other four methods.

Table 3: Results of non-rigid registration for real clinical images.

Methods	Displacement errors		
	e_x (pixel)	e_y (pixel)	e_d (pixel)
PSOBVF	1.877 ± 3.228	1.608 ± 1.622	2.532 ± 3.241
FFD	10.574 ± 4.188	1.170 ± 1.351	10.665 ± 4.278
LDDA	9.461 ± 4.555	1.724 ± 1.219	9.756 ± 4.605
PSOBVF-FFD	1.601 ± 3.478	1.223 ± 0.795	2.011 ± 3.499
PSOBVF-LDDA	1.514 ± 1.516	1.205 ± 0.619	1.928 ± 1.502

Stitching for Real Clinical Images

For 11 pairs of real clinical images, typical stitching results are shown on figure 8 and 9. Figure 8 suggests that our method is capable of stitching three B-mode US scans to form
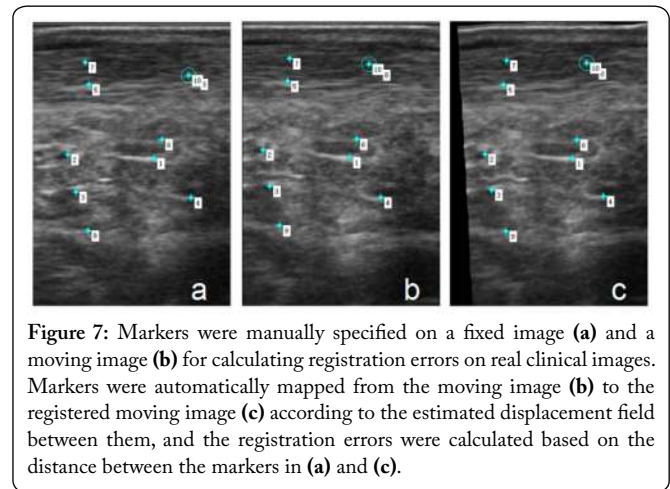

Figure 7: Markers were manually specified on a fixed image **(a)** and a moving image **(b)** for calculating registration errors on real clinical images. Markers were automatically mapped from the moving image **(b)** to the registered moving image **(c)** according to the estimated displacement field between them, and the registration errors were calculated based on the distance between the markers in **(a)** and **(c)**.

a panorama of AT. The entire AT from musculotendinous junction to calcaneal insertion is presented in a single panoramic image. Fig. 9 illustrates two examples of stitching both B-mode and SE images for dual modality visualization of AT with a large field of view. These results demonstrate that our technique can accurately stitch multiple sections of B-mode and SE scans and provide panoramas of AT.
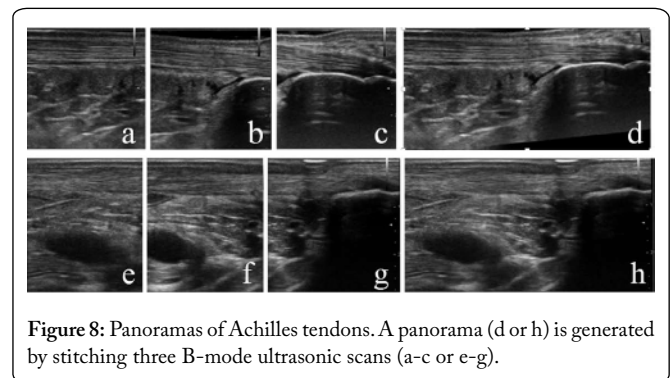

Figure 8: Panoramas of Achilles tendons. A panorama (d or h) is generated by stitching three B-mode ultrasonic scans (a-c or e-g).
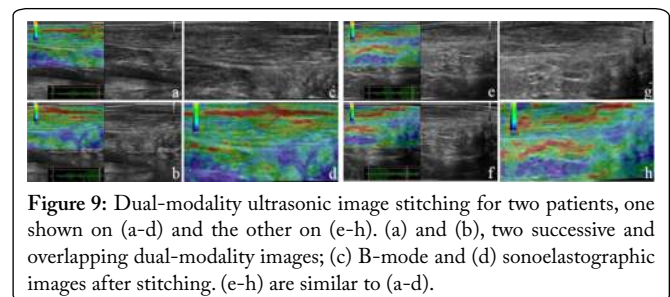

Figure 9: Dual-modality ultrasonic image stitching for two patients, one shown on (a-d) and the other on (e-h). (a) and (b), two successive and overlapping dual-modality images; (c) B-mode and (d) sonoelastographic images after stitching. (e-h) are similar to (a-d).

Discussion

This paper presents a technique for stitching US images of the Achilles tendon, which offers panoramas of AT and would help diagnosis and treatment evaluation of Achilles tendinopathies and tendon ruptures. The technique is currently utilized for offline image analysis, and it is expected to be integrated into commercial US platforms for online clinical examination. Therefore, in daily clinical practice, it might be useful for diagnosing AT injuries, monitoring their progression, and evaluating response of surgical and non-

Image Stitching for Achilles Tendon Ultrasonography Using Particle Swarm Optimization of Boundary Vector Field Based Similarity and Log–Domain Diffeomorphic Registration

Xiong et al.

surgical treatment, including open and arthroscopic surgeries, eccentric training, injections, and extracorporeal shockwave therapy.

In the simulation experiments, the known displacement fields serving as gold standard of registration were employed from simple to complex. First, only a rigid displacement field was applied to an image, which simulated the scenario where two successive ultrasound scans of AT had horizontal and vertical translations. The methods containing a rigid registration step attained better results than the purely non-rigid methods (Table 1). Second, a more complex displacement field was generated by adding non-rigid disturbance to the rigid displacement field to mimic the non-rigid motions of AT during ultrasound scanning. It can be seen from table 2 that the rigid registration method was inferior to the non-rigid methods, and the integration of rigid and non-rigid registration methods had achieved best results, suggesting the superiority of our method.

There is some prior knowledge with regard to tendon motion and tendon texture. For instance, when a tendon is elongated, its thickness will be decreased the derivatives of the horizontal and vertical displacements should have opposite signs. Moreover, the textures of tendon and surrounding tissues appear mainly horizontally oriented (Figure 1d), which maybe provide additional information for image registration. In future studies, the prior knowledge needs to be combined in the registration scheme to ameliorate the image stitching performance.

There are some limitations in this study. First, we only collected the image data of patients with tendon injuries. We will add a control group by recruiting subjects with normal tendons in a future study to evaluate the performance of our methods on both injured and normal tendons. Second, a single radiologist acquired one ultrasound image for one section of an Achilles tendon, and thus the intra- and inter-observer variability could not be assessed. Multiple images of a same tendon section will be acquired by more than one radiologist in the future, and they will be used to quantitatively evaluate intra- and inter-observer variability. Third, intensity variation during US scanning and speckle noise on US images has a great impact on diagnosis. The BVF-based feature space used in our rigid registration step could enhance the edge of the tissue and suppress the speckle noise. It is expected that the statistics of the ultrasonography such as the Rayleigh or Nakagami distributions [31] will be incorporated in the algorithms to further improve the robustness of stitching to the noise and intensity variation.

Conclusions

We have proposed a coarse-to-fine image stitching method for Achilles tendon ultrasonography by integrating BVF, PSO and LDDA. The simulation work and experiments on clinical image stitching demonstrate the high accuracy of the method. It may be potentially used as a tool for future diagnosis and treatment evaluation of Achilles tendon injuries

Conflict of Interest

None

References

1. Holm C, Kjaer M, Eliasson P. 2015. Achilles tendon rupture–treatment and complications: a systematic review. *Scand J Med Sci Sports* 25(1): e1-e10. https://doi.org/10.1111/sms.12209

2. Zwiers R, Wiegerinck JI, van Dijk CN. 2016. Treatment of midportion Achilles tendinopathy: an evidence-based overview. *Knee Surg Sports Traumatol Arthrosc* 24(7): 2103-2111. https://doi.org/10.1007/s00167-014-3407-5

3. Lantto I, Heikkinen J, Flinkkilä T, Ohtonen P, Leppilahti J. 2015. Epidemiology of Achilles tendon ruptures: Increasing incidence over a 33-year period. *Scand J Med Sci Sports* 25(1): e133-e138. https://doi.org/10.1111/sms.12253

4. Magnan B, Bondi M, Pierantoni S, Samaila E. 2014. The pathogenesis of Achilles tendinopathy: a systematic review. *Foot Ankle Surg* 20(3): 154-159. https://doi.org/10.1016/j.fas.2014.02.010

5. Lee KS. 2012. Musculoskeletal sonography of the tendon. *J Ultrasound Med* 31(12): 1879-1884. https://doi.org/10.7863/jum.2012.31.12.1879

6. Zhang ZJ, Ng GY, Lee WC, Fu SN. 2014. Changes in morphological and elastic properties of patellar tendon in athletes with unilateral patellar tendinopathy and their relationships with pain and functional disability. *PloS One* 9(10): e108337. https://doi.org/10.1371/journal.pone.0108337

7. Zhang Q, Cai Y, Hua Y, Shi J, Wang Y, Wang Y. 2017. Sonoelastography shows that Achilles tendons with insertional tendinopathy are harder than asymptomatic tendons. *Knee Surg Sports Traumatol Arthrosc* 25(6): 1839-1848. https://doi.org/10.1007/s00167-016-4197-8

8. Ooi CC, Schneider ME, Malliaras P, Chadwick M, Connell DA. 2015. Diagnostic performance of axial-strain sonoelastography in confirming clinically diagnosed Achilles tendinopathy: comparison with B-mode ultrasound and color Doppler imaging. *Ultrasound Med Biol* 41(1): 15-25. https://doi.org/10.1016/j.ultrasmedbio.2014.08.019

9. Klauser AS, Miyamoto H, Tamegger M, Faschingbauer R, Moriggl B, et al. 2013. Achilles tendon assessed with sonoelastography: histologic agreement. *Radiology* 267(3): 837-842. https://doi.org/10.1148/radiol.13121936

10. Samsudin S, Adwan S, Arof H, Mokhtar N, Ibrahim F. 2013. Development of automated image stitching system for radiographic images. *J Digit Imaging* 26(2): 361-370. https://doi.org/10.1007/s10278-012-9483-5

11. Chang RF, Chang-Chien KC, Takada E, Huang CS, Chou YH, et al. 2010. Rapid image stitching and computer-aided detection for multipass automated breast ultrasound. *Med Phys* 37(5): 2063-2073. https://doi.org/10.1118/1.3377775

12. Ma X, Liu D, Zhang J, Xin J. 2015. A fast affine-invariant features for image stitching under large viewpoint changes. *Neurocomputing* 151: 1430-1438. https://doi.org/10.1016/j.neucom.2014.10.045

13. Liu S, Liu S, Zhang F, Cai W, Pujol S, et al. 2015. Longitudinal brain MR retrieval with diffeomorphic demons registration: What happened to those patients with similar changes? IEEE 12th International Symposium on Biomedical Imaging (ISBI), NY, USA

14. Xia W. and Gao X. 2014. A fast deformable registration method for 4D lung CT in hybrid framework. *Int J Comput Assist Radiol Surg* 9(4): 523-533. https://doi.org/10.1007/s11548-013-0960-1

Image Stitching for Achilles Tendon Ultrasonography Using Particle Swarm Optimization of
Boundary Vector Field Based Similarity and Log–Domain Diffeomorphic Registration

Xiong et al.

15. Zhang J, Wang J, Wang X, Feng D. 2015. Multimodal image registration with joint structure tensor and local entropy. *Int J Comput Assist Radiol Surg* 10(11): 1765-1775. https://doi.org/10.1007/s11548-015-1219-9

16. Singh N, Vialard FX, Niethammer M. 2015. Splines for diffeomorphisms. *Med Image Anal* 25(1): 56-71. https://doi.org/10.1016/j.media.2015.04.012

17. Sum KW, Cheung PYS. 2007. Boundary vector field for parametric active contours. *Pattern Recognition* 40(6): 1635-1645. https://doi.org/10.1016/j.patcog.2006.11.006

18. Studholme C, Hill DLG, Hawkes DJ. 1999. An overlap invariant entropy measure of 3D medical image alignment. *Pattern recognition* 32(1): 71-86. https://doi.org/10.1016/S0031-3203(98)00091-0

19. Chen YW, Lin CL, Mimori A. 2008. Multimodal medical image registration using particle swarm optimization. Eighth International Conference on Intelligent Systems Design and Applications. Taiwan.

20. Wachowiak MP, Smolikova R, Zheng Y, Zurada JM, Elmaghraby AS. 2014. An approach to multimodal biomedical image registration utilizing particle swarm optimization. *IEEE Transactions on Evolutionary Computation* 8(3): 289 – 301. https://doi.org/10.1109/TEVC.2004.826068

21. Chen YW, Mimori A. 2007. Hybrid Particle Swarm Optimization for Medical Image Registration. *Journal of Guangzhou University* 88(3): 517-532.

22. Zhang Q, Wang Y, Yu J, Yang S. 2008. Multimodal medical image registration using geometric flow and Gabor filter. 6th IASTED International Conference on Biomedical Engineering, Austria.

23. Lovbjerg M, Rasmussen TK, Krink T. 2001. Hybrid particle swarm optimiser with breeding and subpopulations. GECCO'01 Proceedings of the 3rd Annual Conference on Genetic and Evolutionary Computation, CA, USA.

24. Lombaert H, Grady L, Pennec X, Ayache N, Cheriet F. 2014. Spectral log-demons: diffeomorphic image registration with very large deformations. *Int J Comput Vis* 107(3): 254-271. https://doi.org/10.1007/s11263-013-0681-5

25. Vercauteren T, Pennec X, Perchant A, Ayache N. 2009. Diffeomorphic demons: efficient non-parametric image registration. *Neuroimage* 45(1 Suppl): S61-S72. https://doi.org/10.1016/j.neuroimage.2008.10.040

26. Curiale AH, Vegas-Sánchez-Ferrero G, Bosch JG, Aja-Fernández S. 2015. A maximum likelihood approach to diffeomorphic speckle tracking for 3D strain estimation in echocardiography. *Med Image Anal* 24(1): 90-105. https://doi.org/10.1016/j.media.2015.05.001

27. Li T, Wang Y. 2011. Biological image fusion using a NSCT based variable-weight method. *Information Fusion* 12(2): 85-92. https://doi.org/10.1016/j.inffus.2010.03.007

28. Szeliski R. 1996. Video mosaics for virtual environments. *IEEE Computer Graphics and Applications* 16(2): 22-30. https://doi.org/10.1109/38.486677

29. Liu D, Wang S, Cao P, Li L, Cheng Z, et al. 2013. Dark-field microscopic image stitching method for surface defects evaluation of large fine optics. *Opt Express* 21(5): 5974-5987. https://doi.org/10.1364/OE.21.005974

30. Liang Y, Zhu H, Friedman MH. 2008. Estimation of the transverse strain tensor in the arterial wall using IVUS image registration. *Ultrasound Med Biol* 34(11): 1832-1845. https://doi.org/10.1016/j.ultrasmedbio.2008.04.005

31. Damerjian V, Tankyevych O, Souag N, Petit E. 2014. Speckle characterization methods in ultrasound images – A review. *IRBM* 35(4): 202-213. https://doi.org/10.1016/j.irbm.2014.05.003